

Sub-Shear Rupture on Bifurcating Faults: Kinematics and Dynamics of the 2021 Mw7.4 Maduo Earthquake in Qinghai

Liuwei Xu¹, Lingsen Meng¹, Chen Ji², Zhang Yunjun³, Eric J. Fielding⁴, Robert Zinke⁴, Han Bao¹

¹Department of Earth, Planetary and Space Sciences, University of California Los Angeles, Los Angeles, CA, USA.

²Department of Earth Science, University of California Santa Barbara, Santa Barbara, CA, USA.

³Seismological Laboratory, California Institute of Technology, Pasadena, CA, USA.

⁴Jet Propulsion Laboratory, California Institute of Technology, Pasadena, CA, USA.

Corresponding author: Lingsen Meng (meng@epss.ucla.edu)

Key Points

- Back projection shows the Mw7.4 Maduo earthquake ruptured bilaterally for ~160 km at sub-shear speeds on an intra-block fault.
- SAR azimuth displacements contribute to the 3D surface deformation and better resolve the slip partition at bifurcating faults.
- Finite fault inversion shows most slip at ≤ 10 km depth, with deep slip in possible ductile layers, indicating tradeoff with crust rigidity.

Abstract

We utilize the slowness-enhanced back projection (SEBP) and joint finite fault inversion (FFI), which combines body waves, surface waves, and 3D ground displacements to image the rupture process and slip distribution of the Mw7.4 Maduo earthquake. The results indicate a 160-km-long bilateral rupture occurring on a north-dipping fault. The WNW branch ruptures a length of ~75 km at 2.7 km/s, while the ESE branch ruptures a length of ~85 km at 3 km/s. Most slip concentrates above 10 km depth, with several major slip patches up to 5.7 m located on the east segment of the main fault and on the bifurcated branching fault. The comparison between SEBP and FFI shows the consistency between large slip pulses and high-frequency sources. We observe up to 3 m slip with large uncertainty in depth beyond 20 km, which is abnormal since it requires rupture penetrating into the ductile layers. We propose that the apparent deep slip could be an artificial compensation to match the observed moment, which indicates

that the crust in the source region is more rigid than the current understanding. Or the deep creeping fault is turned into seismic ones by the strain localization and dynamic weakening. The stress analysis on the forks of the fault demonstrates that the branching behavior on the eastern fork could be well explained by the pre-stress inclination, rupture speed, and branching angle.

Plain Language Summary

A large earthquake struck Maduo county in northeast Tibet on May 21, 2021 with a magnitude of 7.4. To better understand the earthquake rupture and its physics, we use the seismic waveforms from remote seismic stations and 3D surface deformation data from radar satellites to study the rupture geometry, propagation history and the associated slip distribution along the fault. Our results show that the earthquake started at the near-vertical Kunlun Pass-Jiangcuo fault, then propagated bilaterally along the fault for ~160 km at a speed lower than the shear wave velocity. The branching behavior during the rupture propagation can be well explained by the stress direction, rupture speed and angles between forking faults. Combining models from specialized computer code, we find that most slip is concentrated at shallow depth of ≤ 10 km, but there are some moderate slips at depth of > 20 km. The deep slip is abnormal since it requires rupture penetrating into the ductile layers. This indicates either the crust in this region is more rigid than the current understanding, or the deep ductile fault is turned into brittle by the stress change during the rupture.

Index term

Earthquake source observations (1240)

Earthquake dynamics (1242)

Keywords

Finite fault inversion; back-projection; source physics

1.Introduction

The collision of Indian plate and Eurasia plate leads to wide-spread deformation within the Tibet plateau. According to the earthquake focal mechanisms, Yokota et al. (2012) divided Tibetan plateau into four zones according to the focal mechanisms of $M > 4$ earthquakes in the plateau: the northern, eastern, southern, and central zones (Figure 4 in Yokota et al., 2012, also labeled in Figure 1 of this paper). There are mainly reverse dip-slip earthquakes in the northern and eastern zones, and the southern zone is dominated by normal faulting mechanism earthquakes, and in the central zone most earthquakes are strike-slip earthquakes. At 02:04 AM, 22nd, May 2021 of local time, a Mw 7.4 earthquake struck western Maduo county of Qinghai province, a remote area inside the central tectonic zone (Figure 1). The Mw7.4 Maduo earthquake occurred on the middle portion of the E-W oriented sub-vertical Kunlun Pass-Jiangcuo Fault, named in the field investigation after the mainshock. The USGS W-phase focal mechanism (USGS, 2022) indicates it is a left-lateral strike-slip earthquake, reminiscent to the two previous supershear strike-slip earthquakes in Tibet: the 2001 Mw7.8 Kunlun earthquake and the 2010 Mw6.9 Yushu earthquake. The 2001 Mw7.8 Kunlun earthquake ruptured the East-Kunlun Fault, a large and active fault in northern Tibet (Wu et al., 2002). The most distinctive property of the Kunlun earthquake is the supershear rupture speed. Previous studies show that the speed on the center segment of the rupture is between 5 and 6.5 km/s (Vallée and Dunham, 2012; Wen et al., 2009; Robinson et al., 2006). The rupture speed of the 2010 Mw6.9 Yushu earthquake is slightly faster than the shear wave velocity (Yokota et al., 2012; Zhu and Yuan, 2020). The earthquake resulted in severe damage in and around Yushu county, because the ground motion is intensified by the supershear rupture and the Yushu county is located in the frontal rupture direction (Yokota et al., 2012). The Mw 7.8 Kunlun earthquake and the Mw 6.9 Yushu earthquake occurred on the East Kunlun and Ganzi–Yushu faults, respectively, which are the north and the south boundary faults of the Bayan Har block. However, the Kunlun Pass-Jiangcuo Fault, where the Mw 7.4 Maduo earthquake occurred, was in the inner part of the Bayan Har block.

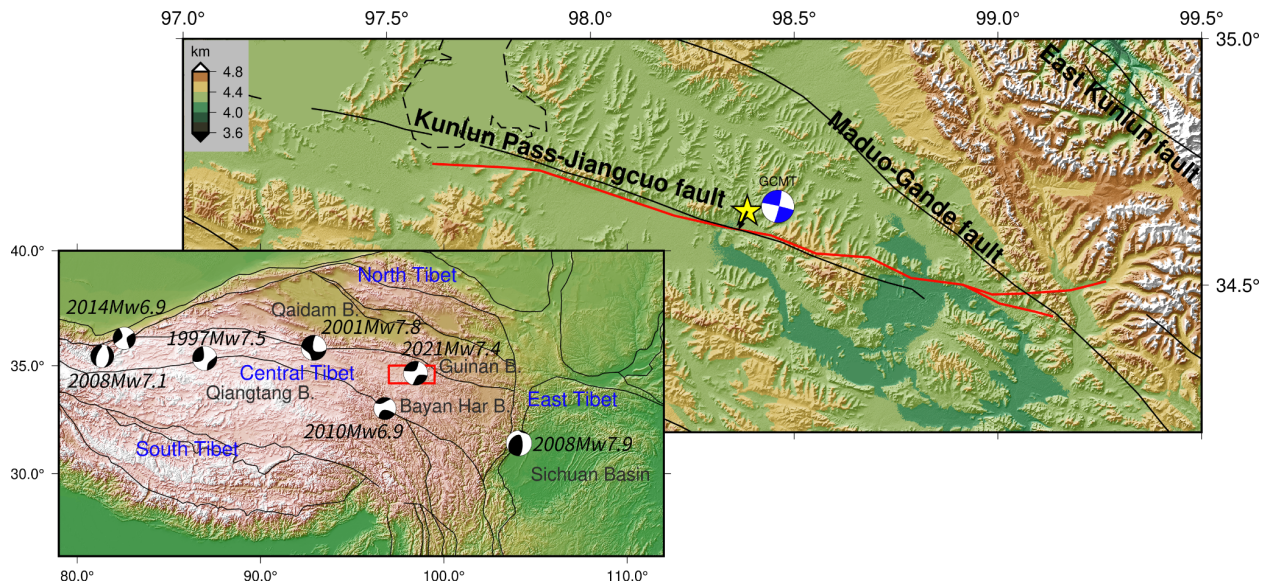


Figure 1. Tectonic setting of the 2021 Mw7.4 Maduo earthquake. The red line denotes the rupture trace mapped using the Sentinel-1 range offsets. The yellow star denotes the hypocenter ($34.650219^{\circ}\text{N}$, $98.384847^{\circ}\text{E}$, depth of 7.6 km, Wang et al., 2021), which is shifted horizontally by 3.9 km following the black arrow to the simplified fault geometry at (34.62°N , 98.37°E) for the purpose of inversion. Black lines denote major faults (GMT China Community, 2021). The focal mechanism and epicenter from GCMT catalog is denoted by the blue beach ball. The low inset shows the major tectonic blocks in Tibetan Plateau and historical significant earthquakes. The red box denotes the study area.

Several studies have investigated the kinematic rupture history of the Maduo earthquake using back-projection and geodetic/seismic finite fault inversions. (e.g. Jin and Fialko, 2021; Chen et al., 2022; Wang et al., 2022; Zhang et al., 2022; Li et al., 2022; Liu et al., 2022). The mutually consistent features of these models suggested the earthquake broke a 150 to 170-km-long fault with a peak slip between 4 m to 6 m observed to the east of the epicenter. Though the Maduo earthquake occurred on a left-lateral strike-slip fault and shared a similar focal mechanism with those two supershear earthquakes mentioned above, the rupture propagated bilaterally, a key difference from the previous two unilateral supershear earthquakes. Previous studies disagreed on whether the Maduo earthquake was a supershear event. Zhang et al. (2022) found a supershear rupture speed of 4 km/s on the eastern segment based on back-projection and far-field Love Mach wave analysis. Yue et al. (2022) proposed the eastward rupture speed was 3-5 km/s according to the back-projection and finite fault inversion. Another back-projection study by Li et al. (2022) suggested that a sub-shear rupture speed was between 1.6-3.0 km/s on the western branch, while the rupture speed of the eastern segment was in the range of 2.72–3.67 km/s. Chen et al. (2022) observed that the fault-normal component of the near-field velocity seismogram from a GPS station located at

eastern of the epicenter was greater than its fault-parallel component, which favored a sub-Rayleigh rupture speed.

In this study, we perform the joint finite fault inversion (FFI) based on Sentinel-1 Synthetic Aperture Radar (SAR) images, body and surface wave data to model the evolution of fault slip on this shallow and long rupture. In addition to the static displacement in range direction utilized in previous studies, we also include the displacement in azimuthal direction into our inversion to constrain the slip distribution on bifurcated fault branches. We also utilize P waveform data from Europe array, Australia array and Alaska array to perform slowness-enhanced back projection (SEBP). Our SEBP calibrates the travel time errors utilizing aftershock locations and subsequently more accurately constrains the rupture length and speed. Bootstrap tests are done to evaluate the spatial uncertainty of SEBP results. We compare the results from SEBP and joint FFI, and find the rupture processes resolved by the two methods are mutually consistent. We investigate the velocity and rigidity properties of the source region crust based on our fault models and some latest tomography studies (e.g. Xia et al., 2021; Han et al., 2021). For ruptures in a complex fault system with multiple branches, fault bifurcation plays an important role in controlling the rupture propagation and branching behaviors. We analyze the dynamic interactions among multiple fault branches according to the strain rate measurement, fault geometry and rupture speeds, which explains the branching behavior during the mainshock. Coseismic slip and aftershock distribution reflect the stress release on the fault during and after the mainshock, respectively. We compare their spatial distribution patterns and discuss their implications for stress release.

2. Finite Fault Inversion

2.1 Seismic Waveform Data

We utilize the joint finite fault inversion (FFI) to image the rupture process and slip distribution on the fault (Ji et al., 2002; 2003). We include 30 broadband body-waves recordings (P and SH, band-pass filtered between 1 and 200 s), 40 long period (3-6 mHz) surface-waves recordings in vertical and transverse components (dominated by Rayleigh and Love wave), and the three-dimensional static displacements derived from Sentinel-1 SAR data in the inversion. The seismic data is recorded at teleseismic distances ($30^\circ < \text{epicenter distance } \Delta < 90^\circ$) and obtained from Incorporated Research Institutions for Seismology (IRIS) data center. The distribution of seismic stations is shown in Figure 2a, and the body and surface waveforms of the selected stations shown in Figure 2b and 2c, respectively.

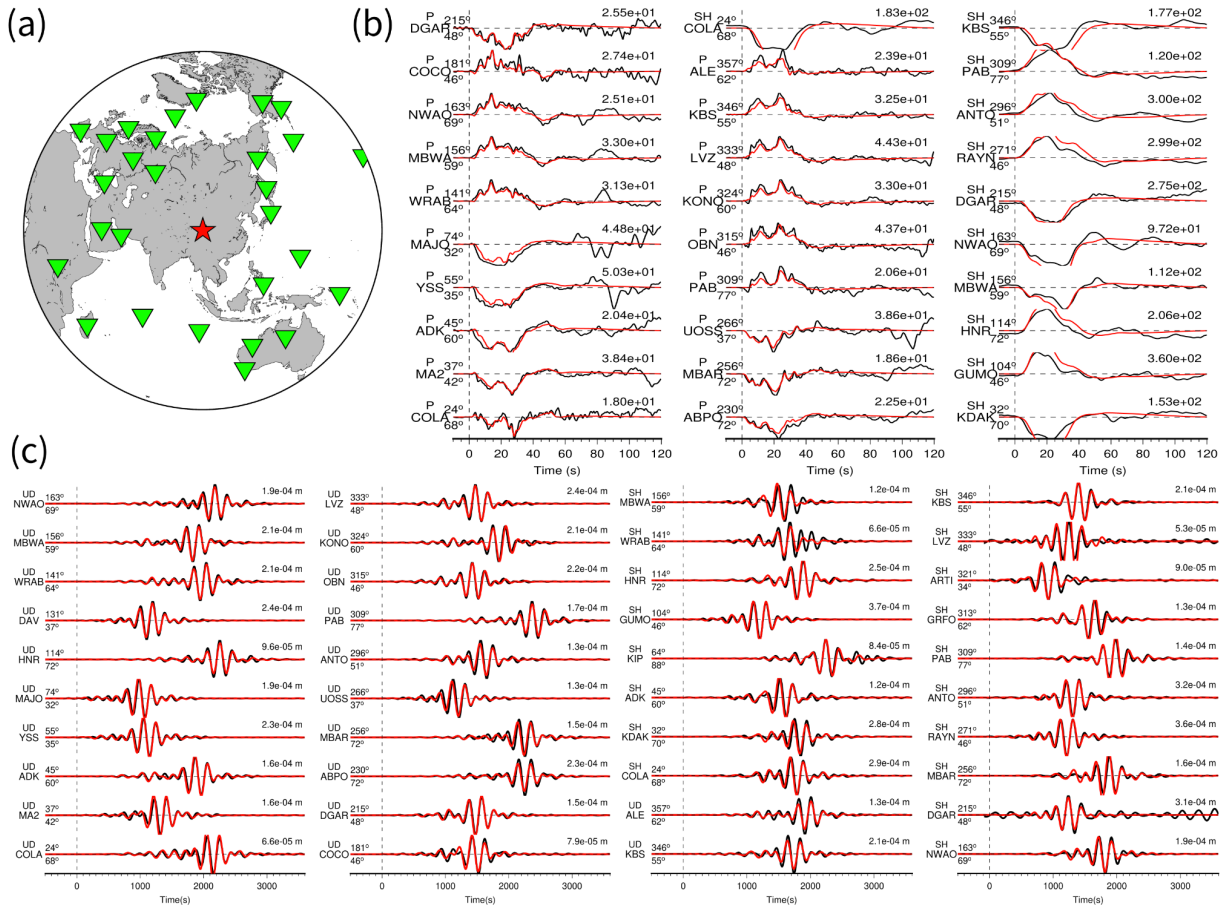


Figure 2. Seismic stations and comparison of teleseismic velocity records (black lines) and synthetic seismograms (red lines) generated by the preferred slip model. **(a)** The station locations. **(b)** The body wave fitting. The wave types and the station names are shown on the left of the waveform. The values on the upper left of the waveforms denote the azimuth. The values on the lower left of the waveforms denote the epicenter distance. The values on the right of the waveforms denote the peak displacement in 10^{-6} m. **(c)** The surface wave fitting. The wave types and the station names are shown on the left of the waveform. The values on the upper left of the waveforms denote the azimuth. The values on the lower left of the waveforms denote the epicenter distance. The values on the right denote the peak displacement.

2.2 SAR Data

We use two pairs of Copernicus Sentinel-1 SAR images (from ascending track 99 and descending track 106, both acquired on May 20 and 26, 2021) to derive the 3D static displacement (Figure 3a and Figure S1) by combining displacements in the range and azimuthal directions from Interferometric SAR (InSAR) and speckle tracking techniques, respectively (Fialko et al., 2001; Fielding et al., 2020), as implemented in the MintPy software (Yunjun et al., 2019). The SAR acquisition time on May 20 and May 26, 2021

tightly bracketed the origin time of the Maduo earthquake (Jin and Fialko, 2021). For the range (cross-track) displacement, we use the ISCE software (Rosen et al., 2012; Fattahi et al., 2017) for interferogram generation with a Goldstein filter strength of 0.5, the minimum cost flow method (Chen and Zebker, 2001) for phase unwrapping guided by a custom mask generated from the spatial coherence with a threshold of 0.4 in the near-fault region (Oliver-Cabrera et al., 2021). We correct for the tropospheric delay using the ERA5 weather reanalysis data (Hersbach et al., 2020) via the PyAPS package (Jolivet et al., 2011). For the azimuth (along-track) displacement, we use the GPU-based PyCuAmpcor package within the ISCE software for the speckle tracking (also known as amplitude cross-correlation or pixel offset tracking). The range offsets are also generated from speckle tracking and used for the surface rupture traces extraction based on their near-field displacement observations, but not used in the slip inversion, in favor for the redundant and more accurate InSAR observations.

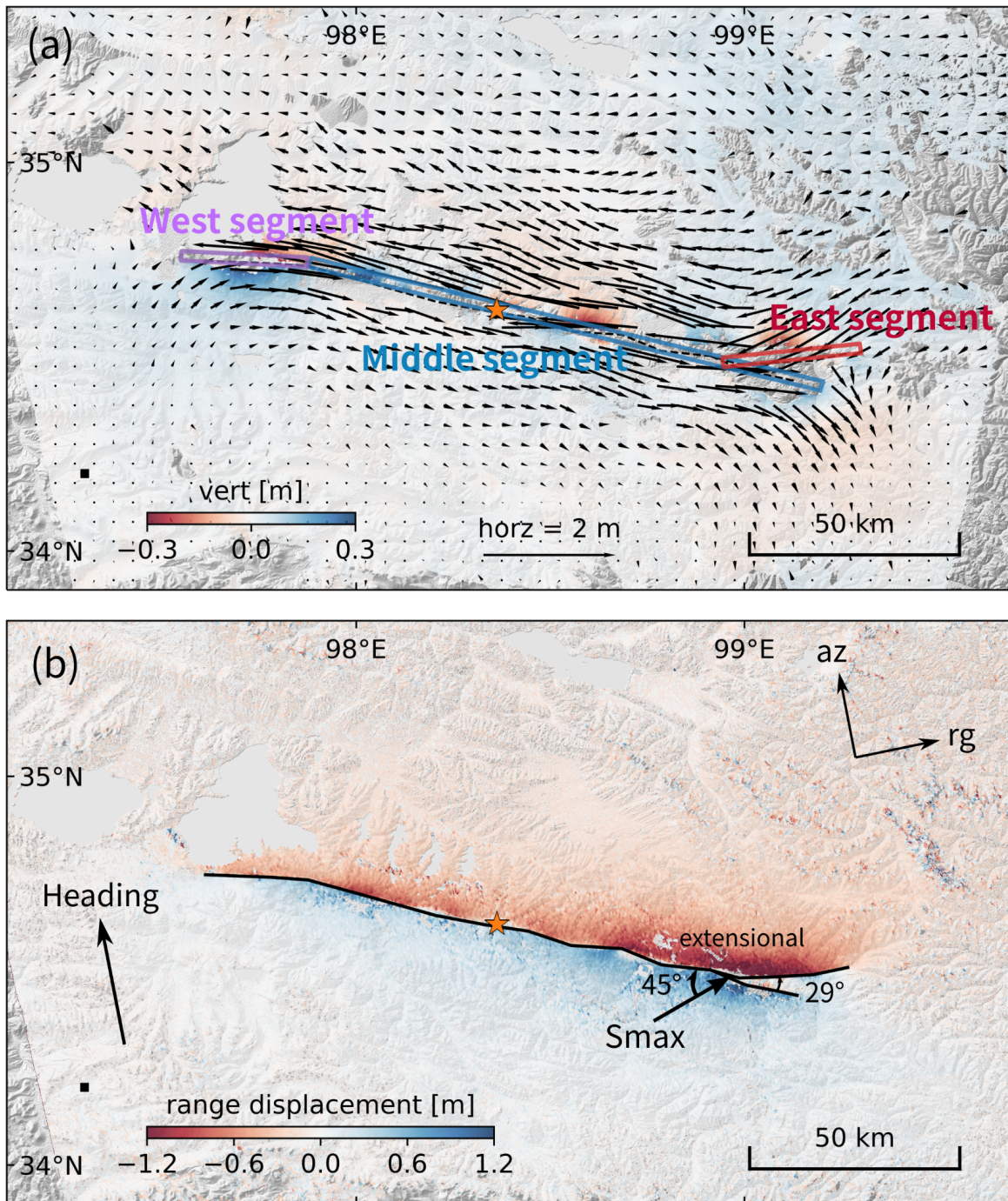


Figure 3. Ground static displacements. **(a)** 3D deformation map for the source region from SAR measurements. The arrows represent horizontal deformation, and the color shows vertical deformation. The red star denotes hypocenter. The purple, blue and red boxes denote the West, Middle and East segments of the fault model. **(b)** The range displacements from speckle tracking along ascending track 099. The surface traces picked based on range displacements are plotted by black lines. Smax is the

maximum compressive principal stress (Wang et al., 2022). Reference point is (34.2°N, 97.3°E), denoted by the small black square.

Considering the lower resolution of Sentinel-1 in the azimuth direction than in the range direction (14.1 m versus 2.3 m), and the relatively small displacement in the north-south direction from this dominantly east-west strike-slip faulting, we use a large estimation window size of 1024 by 512 pixels for the cross-correlation to increase the signal-to-noise ratio (SNR; De Zan, 2014). We correct for the SAR processing effects in the azimuth direction (Gisinger et al., 2021) by estimating a linear ramp for each subswath from the far-field observation and remove it from the entire subswath. For the descending track 106, we apply an extra median filter with a kernel size of 75 pixels to suppress the high spatial frequency noise (Yun et al., 2007). The improvement on the azimuth displacement is shown in Figure S2.

These displacement data are further downsampled with InSamp software (Lohman and Barnhart, 2010; Lohman and Simons, 2005). The maximum displacement recorded in ascending track 099 (AT099) range offset, descending track 106 (DT106) range offset, AT099 azimuth offset and DT106 azimuth offset are 1.36 m, 1.29 m, 1.00 m and 0.82 m, respectively. We trim data points if their shortest distances to the fault surface trace are larger than 50km because of their little influence on the inversion or are less than 2 km to avoid the potential location errors of the picked fault traces (Figure S3) and simplifications in the modeled fault.

2.3 Modeling, Fault Geometry, and Velocity Model

To account for the seismic waveform travel-time errors, we first perform a preliminary FFI based on the arrival time of the P and SH waves predicted using the China Earthquake Administration hypocenter (CEA hypocenter, Wang et al., 2021) and IASP91 1-D velocity model (Kennett and Engdahl, 1991). Then we manually adjust the arrival time so that the predicted waveforms matched the observation. We model the fault plane of the Maduo earthquake with three rectangular fault segments, marked as West segment, Middle segment, and East segment, respectively (Figure 3a). The strikes of these fault segments are extracted based on satellite-based surface traces (Figure 3a,b). We assume these three fault segments share the same fault dip. We conduct a series of preliminary finite fault inversions to search for the optimal dip angle which minimizes the data residue. We find that both seismic and geodetic data favors a slightly north dipping fault geometry. The optimal dip angle is 84° (Figure 4e). We extend these fault planes from the surface to 26 km depth and divide them into 3 km (along fault) by 2 km (along depth) subfaults. We assume the rupture initiates at the CEA hypocenter, which has been shifted horizontally by 3.9 km to match this simplified fault geometry (as shown by the black arrow in Figure 1). Our FFI carries out the

waveform inversion in the wavelet domain and applies a simulated annealing method to simultaneously invert for slip amplitude, rake angle, rupture initiation time, and the shape of an asymmetric function for each subfault (Ji et al., 2002; 2003). Our algorithm combines the body waves, long period surface waves, and static displacements together to estimate the rupture processes of earthquakes and to improve the resolution of focal mechanism and scalar seismic moment of point sources (Ji et al., 2002).

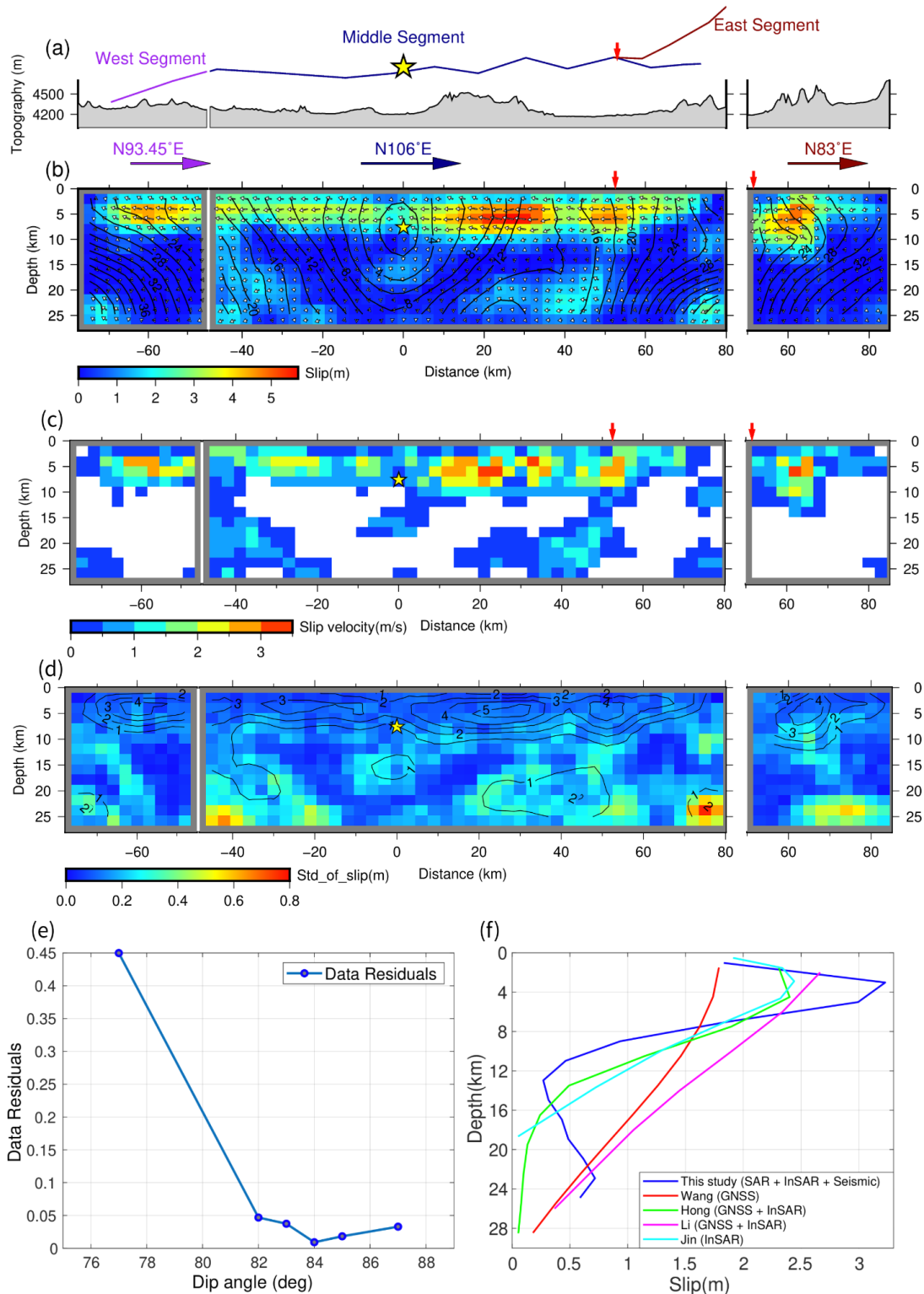


Figure 4. Model of slip distribution on the fault. (a) The fault traces and the topography along fault traces. (b) The preferred model. Red arrows indicate the intersection of Middle and East segments. The color shows the amount of slip, the white arrows indicate the slip vectors, and the contours display the

rupture initiation time. The horizontal arrows and words display the fault orientations. **(c)** Average slip velocity distribution on the fault. Only the subfaults with > 0.57 m slip (10% of the maximum slip) are displayed because the rise time of subfaults with weaker slip is hard to constrain reliably. **(d)** Spatial distribution of the average and the standard deviation of the 10 models. Contours denote the average model and the color denote the standard deviation. **(e)** The relative data residuals as a function of the assumed fault dip angle. **(f)** Along-strike averaged coseismic slip as a function of depth for the 2021 Mw7.4 Maduo earthquake from this and published studies (Wang et al., 2022; Hong et al., 2022; Li et al., 2022; Jin and Fialko, 2021). For clarity, only the names of first authors and the data they used are listed in the label.

The misfit in low-frequency seismic waves is calculated by combining L1 and L2 norms, and that in high-frequency seismic waves is based on the correlation between predicted and observed waveforms (Sen and Stoffa, 1991). This misfit metric is focused on signal shape and is good at capturing the high-frequency and low-amplitude information. For static displacement, the misfit is calculated by the L2 norm. The range and azimuth displacements are weighted based on the reciprocals of observation uncertainty. The inversion aims at minimizing the weighted sum of the seismic and geodetic residue with constraints to minimize the difference between the slip on adjacent subfaults, and to minimize the total seismic moment (Hartzell et al., 1996). The weighting and strength of the constraints is obtained on a trial-and-error basis, balancing the trade-off between the resolution and inversion stability. In our procedure, all inversions begin from random initial fault models with total slip equal to the result of the point source inversions (e.g., Global CMT catalog). The inversions with individual datasets and no constraint are first performed to determine the possible maximum improvements, which are then used to normalize the misfit in the future joint inversion (Ji et al., 2002).

Since the rupture speeds measured by SEBP are 3.0 km/s and 2.7 km/s for eastward and westward rupture propagation, respectively (see Section 3 for more details about SEBP), we allow rupture velocity to vary between 1.5 km/s to 3.5 km/s. We construct a 1D crustal velocity model in the source region (Figure 5a) by interpolating a regional tomography model of northeast Tibet (Xia et al., 2021). The crustal density and shear modulus are inferred from seismic velocity based on the empirical relationships from laboratory measurements (Gardner et al., 1974; Brocher, 2005). This crustal model features a higher velocity upper crust and lower velocity mid-crust compared with the PREM model, consistent with other recent tomography models (e.g., USTClitho2.0, Figure 5a). The synthetic seismograms of body waves and long period surface waves are calculated using first motion approximation (Langston and Helmberger, 1975) and the normal mode superposition algorithm (e.g., Dahlen and Tromp, 1998), respectively. We

implement 800 iterations for each of our inversions. In the final 20 iterations, the misfit oscillation is within $\pm 0.5\%$, suggesting the model has converged to a stable solution.

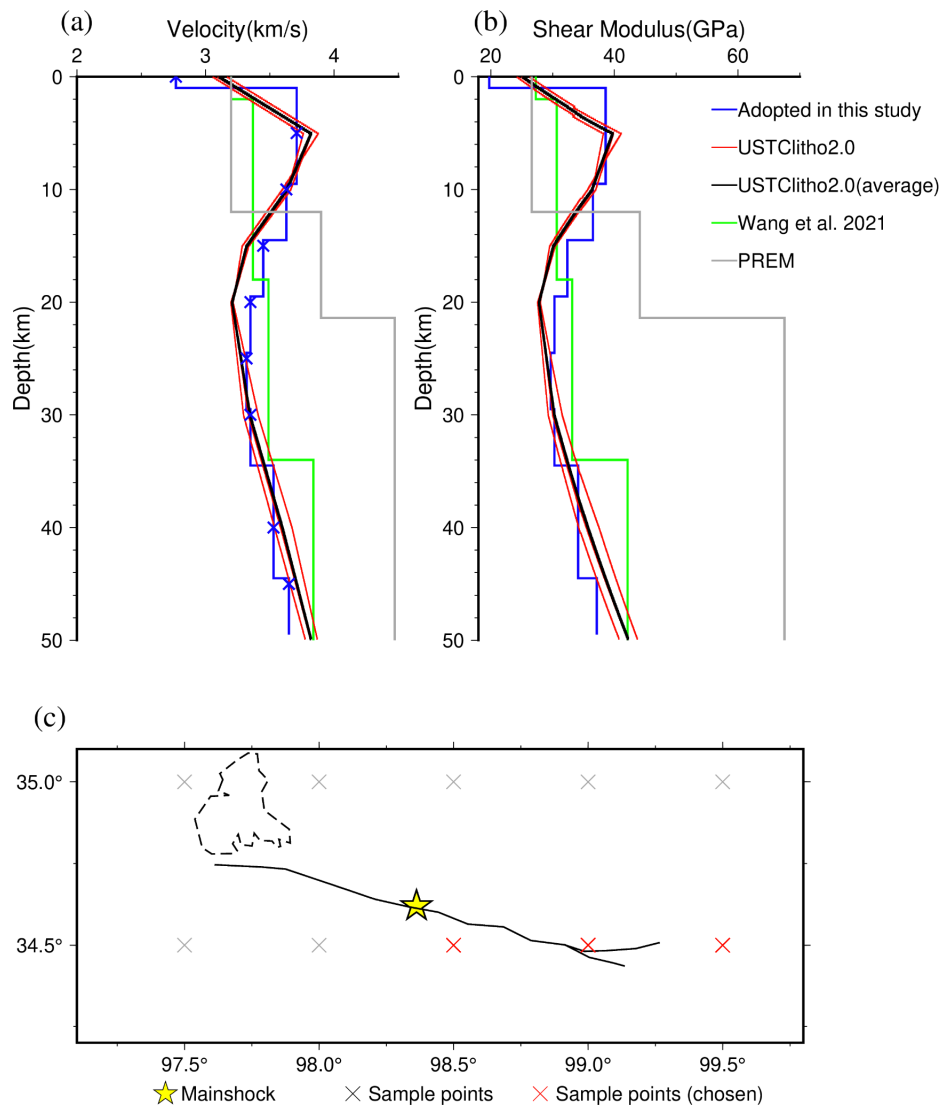


Figure 5. Velocity and rigidity models. **(a)** The velocity models. Different colors denote models from different studies. The black line is the average of the red lines. Crosses on the blue line are the control points from Xia et al. (2021). **(b)** The rigidity models. **(c)** The nodes of the USTClitho2.0 model. Red crosses are three nodes closest to the fault and are corresponding to the red lines in (a) and (b).

2.4 Results

We have conducted 10 inversions with different random seeds. The difference in random seed leads to difference in initial fault model and Markov chain. But we find all inversions reach similar minimum misfits as expected. The standard deviation of the 10 misfits is negligible compared with their average

value ($\sim 0.01\%$ of the average). The inverted model with the smallest misfit is chosen to be the preferred model. Its slip distribution is shown in Figure 4b. Our joint FFI reveals a bilateral rupture, consistent with back-projection results (see Section 3 for more details about BP). The rupture model yields a moment magnitude (M_w) of 7.47. Most of the slip is limited to shallow crust with depth ≤ 10 km. There are two large-slip patches on the eastern Middle segment, centered at 20 km and 50 km away from the hypocenter, with peak slip values of 5.7 m and 4.5 m, respectively. The slip on the western Middle segment is shallower and rather uniform, with an average of ~ 3 m net slip. Significant slip is also seen on the branching faults, with peak slip reaching 4.2 m and 5 m on the West and East segments, respectively. Note that beyond the eastern bifurcation point, the peak slip on the East segment is greater than that on the Middle segment. On the East segment, we observe a minor low-slip zone at the top 2 km, between 50 to 57 km from the epicenter (Figure 4b). The averaged slip as a function of depth is peaked at 3.2 m between the depth of 3-4 km. The averaged slip decreases rapidly from 3.2 to 0.2 m between the depth of 4-12 km but apparently increases slightly from 0.2 to 0.5 m between 15-24 km. Figure S4 shows the sub-sampled data points, predictions of the preferred models, and residuals (the difference between the data and the model predictions) for range and azimuth offsets from ascending and descending tracks. Overall, the preferred model fits the displacement field quite well. Most of the misfit is concentrated near the surface traces and terminal ends, likely due to local undulations of the fault geometry. The misfit for range displacement (from InSAR in both AT099 and DT106) is smaller than that for azimuth displacement (from speckle tracking), because the inversion puts larger weights on the former due to their smaller observational uncertainty.

In addition to the final slip, the distributions of rupture initiation time and average slip velocity are also shown in Figure 4b and Figure 4c, respectively. Based on the rupture initiation time contours, we obtained an average rupture velocity of 2.5 km/s for the eastern propagation and 2.3 km/s for the western propagation, respectively. The average slip velocity is calculated through dividing the final slip by rise time at each subfault. It is noteworthy that to the first order the larger slip correlates with larger average slip velocity. Figure 6 shows the snapshot of the slip in 2 s interval. In the first 20 s, the rupture nucleates at the hypocenter and propagates bilaterally on the Middle segment. At 20 s, both the western and eastern ruptures arrive at the intersections of the branching faults. In the 22-32 s interval, the western rupture steps onto the West segment, while the eastern rupture simultaneously breaks the East and eastern Middle segments. After 20 s, the maximum slip on eastern Middle segment reaches ~ 3 m, while on the East segment the slip reaches ~ 5 m.

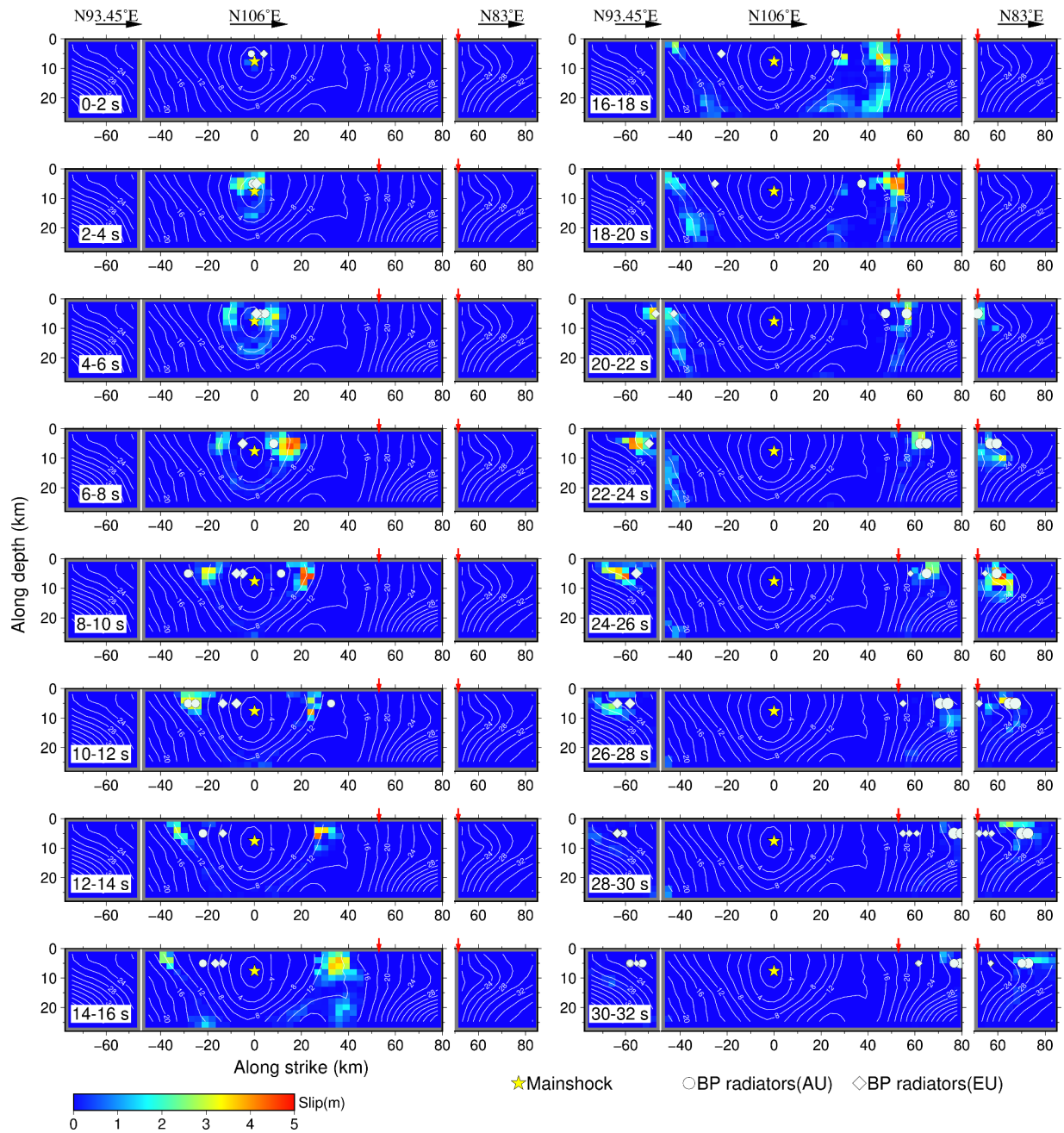


Figure 6. Snapshots of the slip at 2 second time intervals. The numbers at the lower left corner of each panel indicate the time intervals of the snapshots. The yellow star denotes the location of the hypocenter, and white circles and diamonds denote the high-frequency radiators resolved by the Australia array and Europe array SEBP, respectively.

Because our FFI adopted a Monte-Carlo search, the final models vary slightly with different initial guesses. To evaluate the uncertainty of the inversion, we compute the average and the standard deviations of the inverted slip models of those ten inversions (Figure 4d). The mean slip uncertainty of the

mainshock is 0.15 m (2.6% of the maximum slip), though on individual sub faults the uncertainty can be up to 0.8 m (14% of the maximum slip). The standard deviation of inverted fault slip increases with depth. The mean slip uncertainty in the top 10 km is 0.11 m and is approximately 0.15 m between 10-20 km, and rapidly increases to 0.25 m below 20 km (40% of the mean slip below 20 km, Figure S5). The uncertainty analysis demonstrates that our inversion in the shallow portion (top 10 km) is robust, but the slip distribution becomes less well-constrained at the deep faults.

3. Slowness-Enhanced Back Projection

Back-projection (BP) is a popular source-imaging technique that tracks the growth of earthquake ruptures based on coherent seismic wavefields recorded by dense networks (Kiser and Ishii, 2017). Meng et al. improved BP by introducing Multiple Signal Classification (MUSIC) technique (Meng et al., 2011 & 2012), which yielded sharper and more robust source images than the conventional beamforming approach. SEBP improved MUSIC BP by correcting the travel time error in the entire source region caused by heterogeneity of the 3D Earth structure (Meng et al., 2016; Meng et al., 2018 & 2019; Bao et al., 2019). Because the SEBP utilizes the seismic waveforms in higher frequency contents than FFI, the two methods provide complementary views of the earthquake rupture process.

3.1 Data and Processing

SEBP utilizes seismic data in teleseismic distances ($30^\circ < \Delta < 90^\circ$). The data are obtained from Incorporated Research Institutions for Seismology (IRIS) and Observatories & Research Facilities for European Seismology (ORFEUS). For the Maduo earthquake, three large-aperture arrays are available in the teleseismic distance range: Australia (AU, 90 stations), Alaska (AK, 153 stations) and pan-Europe (EU, 401 stations) (Figure 7a). We use the vertical component of broadband seismograms and band-pass filter the seismograms between 0.5 - 2 Hz, the highest frequency range with enough waveform coherence and adequate signal-to-noise ratio. We adopt a 12-s long sliding time window to balance the temporal resolution and robustness. The time step is set to 1 s. Seismograms are normalized by their initial P arrivals so that the amplitude of the waveforms is uniform at all stations.

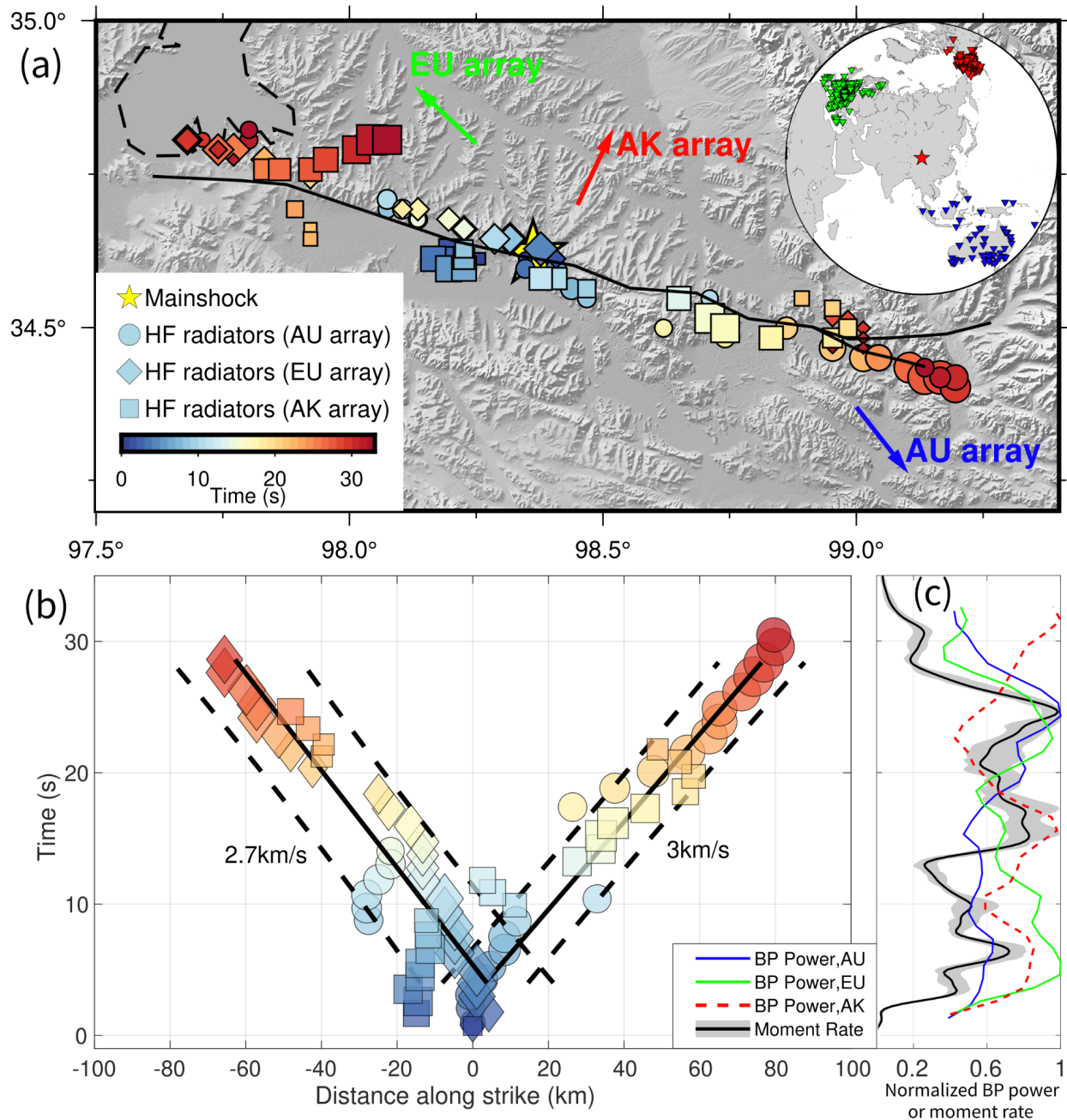


Figure 7. Back-Projection summary. **(a)** The high-frequency (HF) radiators imaged by three arrays. The circles are HF radiators imaged by AU array and color-coded by rupture time. The diamonds are HF radiators imaged by EU array. The squares are imaged HF radiators imaged by AK array. Upper-right inset shows the stations used in SEBP. **(b)** Along-strike location and timing of the radiators. The black solid and dash lines are rupture speeds and uncertainties estimated based on linear regressions of the radiators, respectively. The numbers show the rupture speeds. **(c)** Comparison between BP power and moment rate. The blue line represents the BP power of the AU array. The green line represents the BP

power of the EU array. The red line represents the BP power of the AK array. The gray area is the min/max moment rate from 10 tests, and the black line is the average moment rate.

For large earthquakes, the apparent rupture time is modulated by the rupture directivity. For the receiver station in the rupture frontal direction, the wave train is compressed, and the apparent rupture time becomes earlier than the true rupture time while in the rupture rear direction, the wave train is stretched, which leads to a later apparent rupture time than the true time. Such an effect leads to distorted estimation of source durations and rupture speeds. To correct for the directivity effect, we first calculate the travel time from a given rupture point to the stations, and the travel time from the hypocenter to the stations, then deduct their mean difference at all stations from the apparent rupture time to obtain the true rupture time (Yao et al., 2011; Du, 2021).

To mitigate the travel-time errors caused by 3-D path effects of the Earth structure, standard BP first adopts the travel times predicted by the 1-D reference Earth model (e.g., IASP91, PREM) and then applies the hypocenter correction obtained by cross-correlating the first P phase arrivals (Ishii et al., 2005). However, for large earthquakes, the effectiveness of hypocenter correction decreases when the rupture front propagates far from the hypocenter. In SEBP we apply an additional slowness correction that accounts for the spatial derivatives of the travel times in the source region to reduce the spatial bias and improve the consistency between BP using different arrays (Bao et al., 2019; Meng et al., 2016; Meng et al., 2018).

For the 2021 Mw 7.4 Maduo earthquake, we derived the slowness correction terms based on three aftershocks distributed across the mainshock rupture zone (Figure S6). We choose relatively large aftershocks ($M > 5$) to ensure the initial P waves have enough SNR between 0.5-2 Hz at teleseismic distances. We adopt the CEA event catalog relocated by a double-difference method with 53 stations in 400 km distance range (Wang et al., 2021), so that the earthquake location errors are small enough for a reliable slowness calibration. We compare aftershocks' differential travel times relative to the hypocenter with those predicted by the one-dimensional layered velocity model. The remaining difference of travel-time and the mainshock-aftershock distances are then utilized to solve for the slowness correction terms in a least-squares sense. Figure S6 compares the BP-imaged aftershock locations with and without the slowness correction with respect to the relocated catalog locations: the correction reduced the root-mean-square (RMS) of distance between BP-inferred location and catalog location from 11.92 to 2.03 km, from 2.84 to 1.74 km and from 7.60 to 3.75 km for AU, EU, AK arrays, respectively.

3.2 Results

The results of MUSIC BP enhanced by slowness correction of the arrays are shown in Figure 7. The SEBP radiators of the three arrays are mutually consistent, closely conforming to the surface fault trace. We notice that the Australian array resolves the ESE branch better than the WNW branch, while the European array does the opposite. Such an array-dependent effect is expected for bilateral ruptures: the seismic radiation from the proximal branch dominates and obscures the signal from the far branch (Li et al., 2022). The AK array images both branches equally well because of its sub-perpendicular orientation to the fault strike. The SEBP identifies coherent sources for approximately 32 s after the rupture initiation. The rupture propagates bilaterally, extending in the ESE-WNW directions. The WNW branch breaks a 75-km-long segment while the ESE branch ruptures a 85-km-long branch. Figure 7b plots the along-strike BP locations versus rupture time. The rupture initially stagnates near the hypocenter for ~ 4 s, and then propagates bilaterally at stable speeds for ~ 28 s. During the stable propagation stage, the average rupture speed for the west and east branches is 2.7 km/s and 3 km/s, respectively.

3.3 Uncertainty Analysis

To estimate the uncertainty caused by coda waves, local scattering, and heterogeneous site effects, we bootstrap the BP by adding randomized noise to the signal. The noise amplitude spectrum is estimated based on the incoherent part of the waveforms. First, a reference point-source location at each time step is defined by the peak of the BP image. At each time window, we obtain the mean seismogram (as a proxy of the coherent arrival) by aligning, stacking, and averaging the array waveforms according to the time shift predicted by the reference location. The incoherent noise at each station is computed as the waveform residual with respect to the mean seismogram. The noise is shuffled by randomizing its Fourier phase spectrum, and added back to the mean seismogram. This procedure is designed to model the random phases of scattering waves while retaining the amplitude spectrum of the waveform. One hundred synthetic realizations of the mean seismogram plus incoherent noise are then back-projected to obtain the perturb BP locations for each time step. Figure 8 shows the ellipses representing the 95% confidence-bound on the BP radiator locations. We find that the major axes of the uncertainty ellipses are generally pointing toward the receiver array, indicating a greater uncertainty along the radial direction (toward the array) than the tangential direction. The median length of the major and minor axes are 1.5 by 0.6 km, 3.3 by 0.4 km and 3.7 by 1.8 km for AU, EU and AK array, respectively. These analyses suggest that the uncertainty of the three arrays are reasonably small. Among them, the AU BP is the most reliable probably due to its largest array aperture; The EU BP has a small tangential uncertainty but a moderate radial uncertainty; The AK BP has moderate uncertainty in both the radial and tangential directions. We

note the uncertainty becomes much larger near 32 s for the EU and AK BPs, which indicates that the coherent waveform is diminishing and incoherent coda starts to dominate the wavefield. Therefore we consider the rupture duration determined by SEBP is 32 s, consistent with the rupture duration derived by FFI.

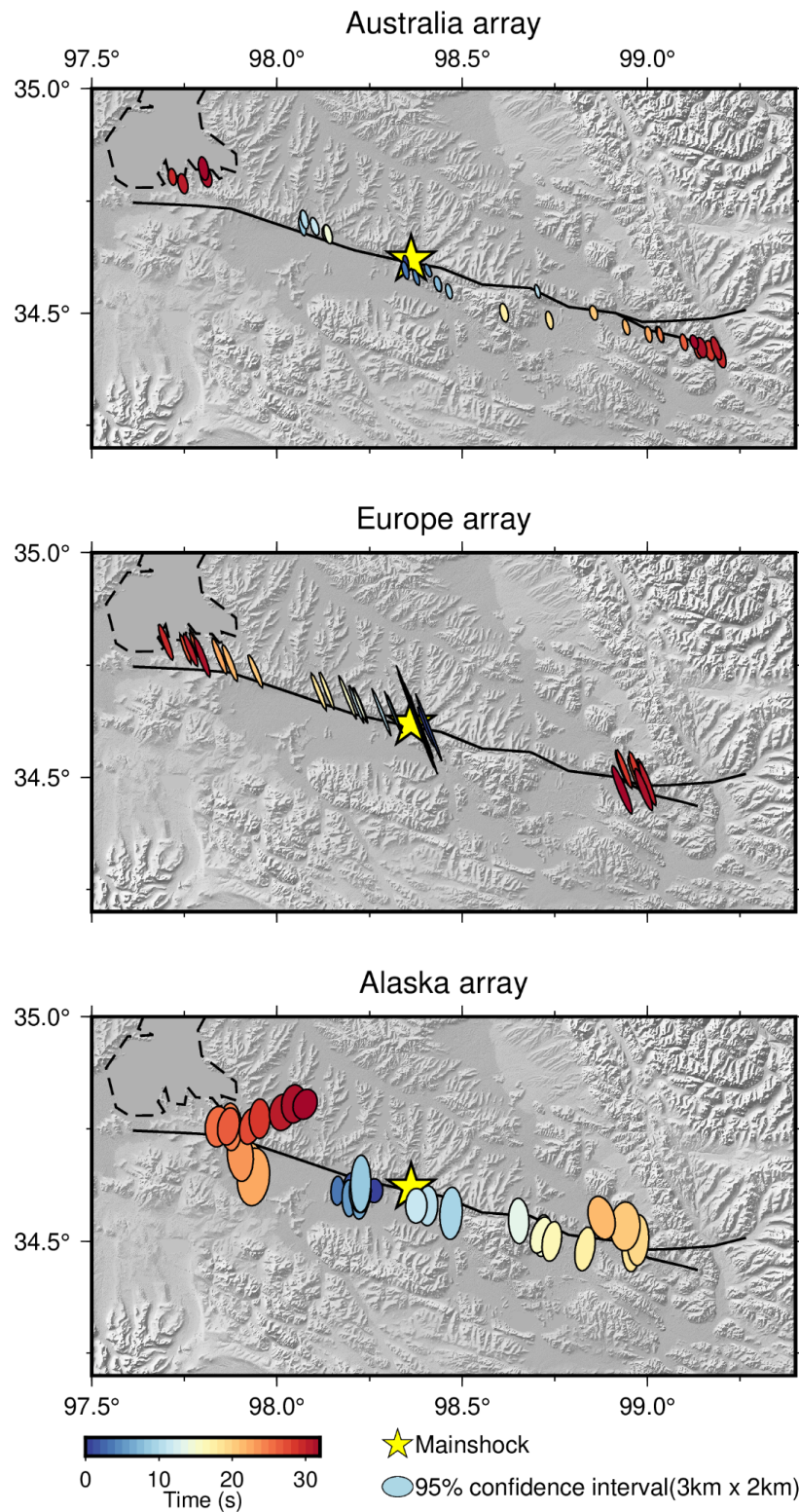


Figure 8. Uncertainties of AU, EU, and AK arrays. The colors and shapes of the ellipses demonstrate the BP timing and the 95% confidence interval on the peak locations. The ellipse in the legend demonstrates

the uncertainty with 3 km in the major axis and 2 km in the minor axis. The yellow stars indicate the epicenter.

4. Discussion

4.1 Tradeoff between the deep slip and shallow rigidity

We compile published fault models of this earthquake (Wang et al., 2022; Hong et al., 2022; Li et al., 2022; Jin and Fialko, 2021) and plot average slip as a function of depth (Figure 4f). These models are derived from multiple datasets (e.g. SAR, InSAR, GPS, seismic waves) and are mutually consistent overall: The maximum coseismic slip occurs in the uppermost crust, in the depth interval of 1–4 km below Earth's surface; the average slip decreases beyond 4 km depth. However, there is a significant difference in the maximum average slip, which varies from 1.7 m to 2.7 m, and a wide range of the depth extent of the coseismic slip from 19 km to 28 km. In our preferred model (the blue line in Figure 4f), the slip reaches the peak at 3–4 km depth, with a maximum average slip of ~3.2 m. The slip decreases rapidly between 4–13 km depth but increases between 13–24 km. This increase is not seen in any other models.

It requires extra caution to determine if the deep slip is real or not. The 2001 Mw7.8 Kunlun earthquake only had a depth extent of 20 km, while the length exceeded 400 km (Lasserre et al., 2005; Robinson et al., 2006). Mechie et al. (2004) revealed that the 700°C isotherm was likely to be at a depth of 18 km in central Tibet, as the lower crust had been warmed as a result of burial and radioactive decay in the crust. Huang et al (2009) inferred a laterally extensive ductile flow between depths of 16–26 km at Songpan-Ganze block, which was closely located on the southeast of the Maduo earthquake source region. According to the above studies, the deep slip in our model is probably abnormal since it requires rupture penetration into the ductile layer.

One plausible explanation is that the deep slip is an artificial compensation to match the observed moment constrained by the long-period surface waves. On a given fault plane, the total moment is the product of the fault slip, fault area and rigidity (shear modulus) of the surrounding rock. If the assumed shear modulus is lower than its true value, the inversion generates artificial slip to compensate for the seismic moment. Since the shallow slip is well constrained by the geodetic data, the extra artificial slip tends to be mapped into the less-well constrained deep fault. The averaged standard deviation of inverted slip below 20 km is 0.25 m (40% of the mean slip below 20 km, Figure S5), which shows that the slip at the deep fault is less well-constrained. In ten inversions, the average moment contributed by the deep slip is 23% of the total moment, with the standard deviation being 2.4% of the average deep moment. Though the

shapes of deep slip pockets are not well constrained, the overall contribution to the seismic moment is robust and significant. In our inversion, the crustal density and shear modulus are inferred from shear wave velocity (V_s) based on the empirical relationships from laboratory measurements (Gardner et al., 1974; Brocher, 2005), therefore the V_s adopted in our inversion can be viewed as a proxy for the shear modulus. Since most of the coseismic slip is in the upper 10 km, the V_s and hence the shear modulus in that depth range has the greatest impact on the seismic moment.

To explore the sensitivity of deep slip to V_s , we compare the inversion results using different V_s models. The 1-D V_s structure we adopted in the preferred model is relatively fast in shallow crust (Figure 5a and 9d). We conduct another inversion using a slower V_s model (Figure 9d, the one adopted in the aftershock relocation study, Wang et al., 2021). After switching from the fast to slow V_s model, the average slip in the shallow part (depth ≤ 10 km) only changes from 2.13 m to 2.11 m, while the slip in the deep part (depth > 10 km) increases from 0.45 m to 0.59 m (Figure 9e). It demonstrates that the slip above 10 km is stable and insensitive to the variation of V_s , while the deep slip is negatively correlated with the V_s and hence the shear modulus in the shallow depth. In other words, a lower V_s in the shallow part will result in a larger artificial deep slip. Some of the latest tomography studies in northeast Tibet or continental China (Xia et al., 2021; Han et al., 2021) do show higher velocity than that of PREM in the top 10 km in the source region (Figure 5a). However, the existence of the deep slip in the preferred model indicates that true V_s might be even larger than Xia and Wang models. The inaccuracy of velocity models is not surprising because no near-field seismic stations were deployed in the source region until the Mw7.4 Maduo earthquake.

However, without an accurate velocity model, we cannot exclude the possibility that the deep slip is real. The aftershock relocation study showed some events occurred on the deep fault (depth ≥ 20 km) with magnitude up to 3.8 (Wang et al., 2021). Recent laboratory experiments (Toro et al., 2011) and theoretical studies (Rice, 2006) indicated that at slip rates of $\sim 10^{-1}$ m/s and higher, the earthquake rupture behavior could be controlled by enhanced dynamic weakening of fault frictional resistance. During an earthquake, when the rupture reached deep fault extensions, increased strain rate and shear heating could result in strain localization and dynamic weakening (Platt et al., 2014), effectively turning the creeping fault zones into seismic ones (Noda and Lapusta, 2013). Jiang and Lapusta (2016) also proposed that for large strike-slip earthquakes, rupture could penetrate below the seismogenic zone and reach the deep part of the fault.

Above analysis of the shallow velocity (rigidity) and deep slip shows the power of joint FFI: if we know the exact depth extent of the slip through some prior information, we could compare the inverted slip depth with the actual depth and check the accuracy of the velocity model. On the other hand, the joint FFI is able to examine the existence of slip at great depth, even though the constraint for the deep slip is not as good as that for the shallow one and the deep slip is possibly in the ductile zone.

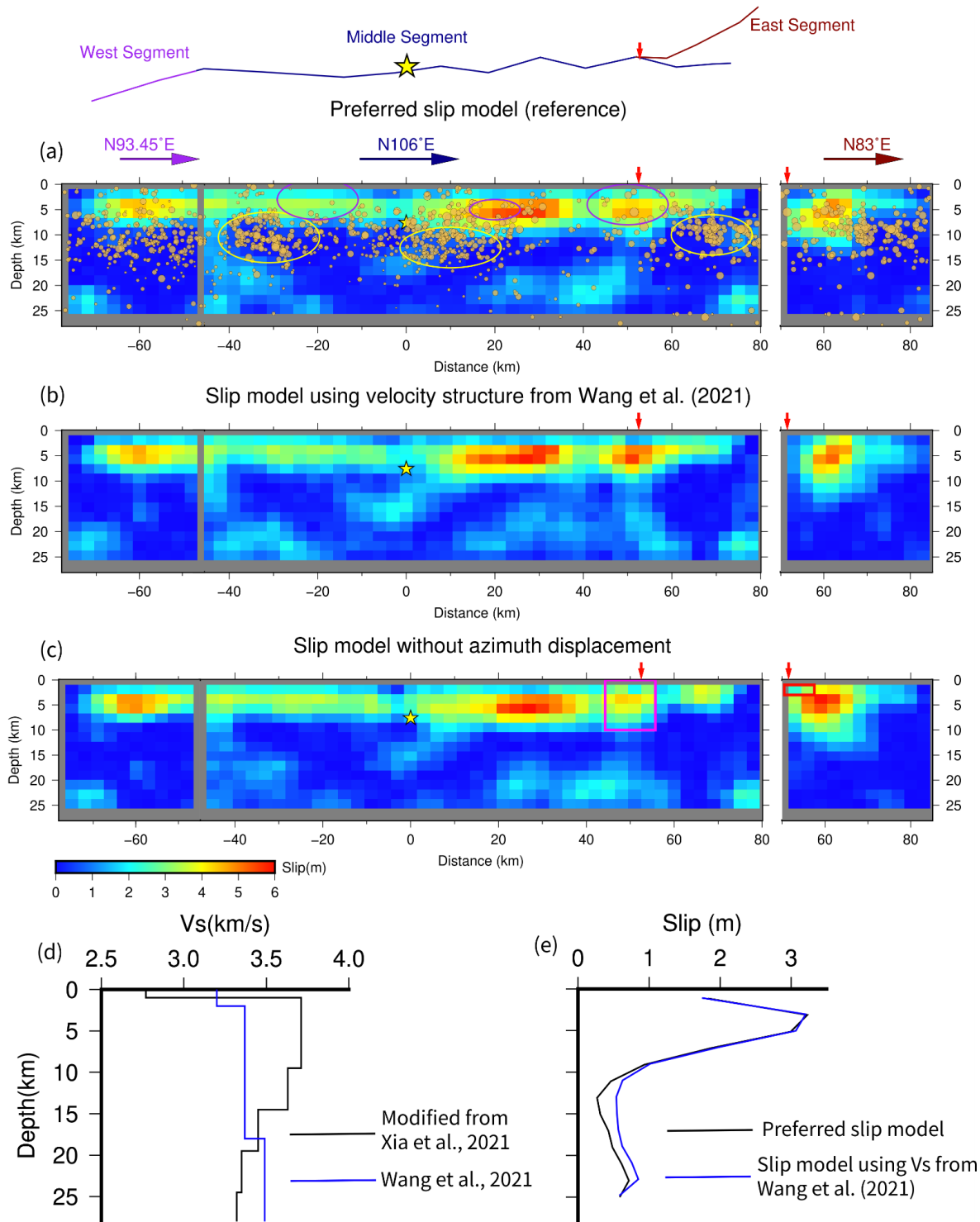


Figure 9. Comparison between slip models inverted with different 1-D Vs structures and with different displacement data. (a) The preferred model inverted with 1-D velocity structure modified from Xia et al. (2021). The light brown points denote the aftershocks and the size is proportional to the magnitude. The purple ellipses highlight the region with sparse aftershocks. The yellow ellipses highlight the region with

dense aftershocks. The red vertical arrows denote the connecting points of Middle and East segments. **(b)** The model inverted with 1-D velocity structure the same as Wang et al., (2021). **(c)** The slip model inverted without azimuth displacement data. The magenta and red boxes denote the compared regions mentioned in section 4.3. **(d)** Comparison of the V_s structure adopted in the preferred model (modified from Xia et al., 2021, the black line) and the V_s structure adopted in Wang et al. (2021) (the blue line). **(e)** Comparison of the along-strike averaged slip as a function of depth. The black line represents the slip of the preferred model, and the blue line represents the slip of the model using V_s from Wang et al. (2021).

4.2 Kinematics of the sub-shear ruptures

We observe remarkable consistency between the high-frequency sources resolved by BP and the areas of large slip resolved by FFI in Figure 6 and Supplementary Movie S1. Such consistency indicates collocation of high-and-low-frequency seismic radiation. The BP power and the moment rate function also support the consistency (Figure 7c). There are two maxima in the BP power of AU and EU arrays: one at ~ 6 s and another at ~ 25 s. In the corresponding time windows, we also observe the peaks of the moment rate function.

The rupture speed is an important parameter of source kinematics. One outstanding question for the Maduo earthquake is whether the rupture speed is super-shear, similar to its sibling large strike-slip earthquakes on the Tibet plateau, the 2001 M 7.8 Kunlun and 2010 M 6.9 Yushu earthquakes. Our SEBP shows that during the bilateral propagation stage, the average rupture speed for the west and east branches is 2.7 km/s and 3 km/s, respectively, which are approximately 73% and 81% of the local V_s of 3.7 km/s in the shallow crust. Considering the possible underestimation of V_s discussed in Section 4.1, this ratio might be even lower.

Our estimates are consistent with that from the BP study by Li et al. (2022), which found the rupture speed for the east segment was in the range of 2.72–3.67 km/s and the speed for the west rupture was in the range of 1.39–1.78 km/s in the first 20 km and then increased to 2.82–3.17 km/s. While most BP and finite fault models suggest sub-shear rupture speed (Chen et al., 2022; Li et al., 2022), one particular BP study combining multiple teleseismic arrays claims the rupture speed of the east branch reaches a supershear speed of 4 km/s (Zhang et al., 2022). We don't agree with the supershear claim due to the following reasons:

1. A close examination of Figure 2 and S4 of their paper suggests that the combined BP for the east branch is dominated by the AU array, which is the only one showing a supershear speed. Our SEBP indicates the speed of the east branch inferred from the AU array is also overestimated

before the slowness calibration (3.2 km/s vs 3.0 km/s) (Figure S7b and Figure 7b). Therefore, it is possible that the apparent supershear speed observed in Zhang et al.(2022) is a result of the path effect of the AU array.

2. The supershear rupture speed is contradictory with the analysis of near-field ground motions (Chen et al., 2022). They found the greater fault-normal component than the fault-parallel component in the velocity seismogram recorded in a near-field station located at east of the epicenter, indicating a sub-Rayleigh rupture speed.
3. As mentioned in the Introduction, the 2001 Mw7.8 Kunlun and the 2010 Mw6.9 Yushu earthquakes were on the East Kunlun and Ganzi–Yushu faults, respectively, which are the northern and southern boundary faults of the Bayan Har block. Interseismic GPS velocity data (Wang and Shen, 2020) illustrates greater tangential velocity gradient across the East Kunlun and Ganzi–Yushu faults than that in the interior of the Bayan Har block (Wang et al., 2022). Along the block boundary, the long term slip rate is generally larger than what is inside. Large slip rates lead to smoothing and mature faults, which is one major condition of super-shear rupture (Perrin et al., 2016). However, the 2021 Maduo earthquake occurred on the intra-block Kunlun Pass–Jiangcuo fault, which is less mature and not suitable for super-shear rupture to develop.

The aftershocks carry key information about the stress release during the coseismic and postseismic slip processes. Wang et al. (2021) performed a relocation study for the aftershocks of the Mw7.4 Maduo earthquake. They relocated all positive-magnitude aftershocks within 8 days after the mainshock. We shift the relocated aftershocks horizontally to our fault planes (Figure 9a) and find the aftershocks are noticeably less common in the principal-slip area (purple ellipses in Figure 9a). On the other hand, we observe dense aftershocks at the edges of large-slip patches (yellow ellipses in Figure 9a). This is a common feature of many other earthquakes (Mendoza and Hartzell, 1988; Kato et al., 2010; Kato and Igarashi, 2012). The decoupling of large-slip and aftershocks suggests: the press-stress is released by the mainshock; The coseismic slip casts a stress shadow prohibiting the aftershocks; The residue stress concentrates at the edge of the large-slip zones, and is released by the aftershocks and possible afterslip.

4.3 Constraint on the slip partition from the azimuth displacement

With a striking angle of $\sim 106^\circ$, the static displacement of the Maduo earthquake is primarily oriented in the E-W direction. However, the eastern fault bifurcation introduces the large fault-normal displacement in the N-S direction (Figure S1), which is only measurable using the azimuth offsets due to the imaging geometry of polar-orbiting SAR satellites. Previous studies (Jin and Fialko, 2021; Chen et al., 2021; Li et al., 2022; Zhang et al., 2022; Hong et al., 2022) use only the static displacement in the range direction

from InSAR or speckle tracking, or with spatially sparse azimuth measurement from Sentinel-1 burst overlap interferometry (Liu et al., 2022). We adopt extra procedures (section 2.2) to obtain a spatially continuous and high SNR azimuth offset at the cost of reducing spatial resolution (Figure S2).

To see how the inversion is improved by the azimuth offset data, we perform an additional inversion without the azimuth offset and compare the result with the preferred model. Figure 9a and 9c show the change of slip partition between the two branches near the junction: With the azimuth displacement data included, the maximum slip on the East segment decreases from 5.9 m to 4.9 m, while the average slip around the junction (magenta boxes in Figure 9c) on the Middle segment increases from 2.8 m to 3.1 m. Another distinct difference is that the shallow slip of the East segment near the fault junction (red boxes in Figure 9c) decreases from 3 m to 1 m when including azimuth offsets. The smaller shallow slip indicates that the rupture steps onto the East segment through the deep (>2 km) rather than near-surface portion (<2 km) of the fault. The involvement of azimuth offsets in the FFI of the Maduo earthquake demonstrates that for earthquakes rupturing complex fault systems, the static deformation data in both range and azimuth directions should be included into the inversion to better constrain the slip distribution.

4.4 Rupture dynamics on bifurcating faults

The range offset map (Figure 3b) and the aftershock locations (Figure 8 of Wang et al., 2021) reveal that the Kunlun Pass-Jiangcuo fault is bifurcated at the eastern end during the Maduo earthquake. According to the pattern of surface deformation, the rupture propagates on both the main fault (Middle segment) and branching fault (East segment). The branching fault is on the extensional side according to its orientation and the left-lateral motion. Rupture bifurcation is a complicated issue and has been investigated by both theoretical and numerical studies. In the 2001 Kunlun earthquake, a fault bifurcation near the Kunlun Pass fault is responsible for slowing down the rupture (Robinson et al., 2006). Kame and Yamashita (1999a; 1999b) showed that the dynamic growth of a rupture tends to be arrested soon after the bifurcation because the level of stress concentration at the rupture tip is reduced after the bifurcation. According to the rupture dynamic simulation studies (Kame et al., 2003; Bhat et al. 2007), whether rupture can continue beyond the bifurcation point depends on the inclination of the maximum pre-compression (S_{max}), the rupture velocity (V_r) and the branching angle (θ , angles between the main and branching fault).

We find Kame et al. (2003) simulation results applicable in explaining the branching behaviors of the Maduo earthquake. Figure 3b shows that at the eastern fork, the inclination of S_{max} inferred from GPS strain rate measurement (Wang et al., 2022) and fault geometry is $\sim 45^\circ$ (intermediate inclination), with the

θ being $\sim 29^\circ$. According to Kame et al. (2003), under the intermediate inclination of S_{\max} , the most favorable plane to slip is on the extensional side and 3° deviates from the main branch. Under this pre-stress condition, the failure on the main fault is dynamically self-chosen and simultaneous rupture on both main fault and branching fault is possible. Meanwhile, the BP-inferred V_r is $\sim 3\text{km}$ ($\sim 0.8 V_s$), which is fast enough and causes high dynamic stressing to drive the rupture after bifurcation on both faults. The wide branching angle θ makes rupture on both faults less affected by stress interaction thus reducing the stress shadow effect (the stress release around one fault discourages the failure on vicinity fault).

5. Summary and Conclusions

In this study, we utilize SAR static surface displacements, SEBP, and joint FFI to explore the kinematic rupture history of the 2021 Mw7.4 Qinghai Maduo earthquake. The fault surface trace indicates there is a bifurcation near the eastern terminal end of the rupture. By Including the azimuth offsets derived from SAR images, our inversion improves the constraint on the slip partition on bifurcated fault branches. Both SEBP and FFI resolve a bilateral and sub-shear rupture, breaking a west branch of 75 km and an east branch of 85 km. The BPs of all three arrays (AU, AK, and EU) are mutually consistent and their location errors are rather small. The consistency between SEBP and FFI indicates collocation of high-and-low-frequency seismic radiation. We find most of the slip is distributed within the top 10 km, which is well constrained by joint FFI according to our uncertainty analysis.

The excessive deep slip in the FFI result is abnormal because it is probably in the ductile layer. We propose two explanations for the deep slip: the deep slip could be an artifact to compensate for the observed moment, which indicates the velocity and shear modulus of the source region are larger than those values in published tomographic studies. Or the deep creeping fault is activated seismically by the strain localization and dynamic weakening, thus being able to host the brittle slip. We find the branching behaviors at the eastern fork fit the previous simulation results well. The intermediate principal pre-stress inclination and the fast rupture velocity allow the rupture on the branching fault and the main fault to develop, and the wide angle between forking faults reduces the stress shadow effect.

Acknowledgment

This work is supported by the NSF CAREER grant EAR-1848486 and the Leon and Joanne V.C.Knopoff Fund. Part of this research is performed at the Jet Propulsion Laboratory, California Institute of

Technology under contract with the National Aeronautics and Space Administration (80NM0018D0004) and supported by the Earth Surface and Interior focus area. We thank L. Shi for sharing the velocity model of northeast Tibet, W. Wang for sharing the aftershock catalog, and Z. Jin, S. Hong, C. Xu, J. Geng, and Q. Li for sharing their slip models. We thank Z. Jin for fruitful discussions. The broadband seismograms are provided by the Incorporated Research Institutions for Seismology (IRIS, www.iris.edu) and Observatories & Research Facilities for European Seismology (ORFEUS, www.orfeus-eu.org). The Python software package Obspy (www.obspy.org) is used for data requesting, waveform filtering, and cross-correlation processing. This work contains modified Copernicus data from the Sentinel-1A and -1B satellites provided by the European Space Agency (ESA). Figures are produced using Generic Mapping Tools (GMT) (Wessel et al., 2013), Matlab, Matplotlib and Cartopy. The static displacement data is downsampled by InSamp (<https://github.com/williamBarnhart/InSamp>).

Data Availability Statement

The Copernicus Sentinel-1 data are made available by the ESA and mirrored by the Alaska Satellite Facility (ASF; <https://www.asf.alaska.edu/sentinel/>). The InSAR Scientific Computing Environment (ISCE) software used for processing the Sentinel-1 SAR data is available at <https://github.com/isce-framework/isce2>. The moment tensor solutions come from the U.S. Geological Survey (USGS; <http://earthquake.usgs.gov>) and the Global Centroid Moment Tensor project (CMT; <http://www.globalcmt.org>). The teleseismic data and surface wave data used in this study come from the IRIS Data Management Center (http://ds.iris.edu/wilber3/find_event) and Observatories & Research Facilities for European Seismology (ORFEUS, www.orfeus-eu.org). The relocated aftershock data is from Wang et al. (2021), which can be accessed through <https://doi.org/10.1007/s11430-021-9803-3>. The USTClitho2.0 model is from Han et al. (2021), which can be accessed through <https://doi.org/10.1785/0220210122>. The velocity model of northeast Tibet is from Xia et al. (2021), which is obtained through the request to the corresponding author.

Reference

- Bao, H., Ampuero, J. P., Meng, L., Fielding, E. J., Liang, C., Feng, T., & Huang, H. (2019). Early and persistent supershear rupture of the 2018 Mw 7.5 Palu earthquake. *Nature Geoscience*, 12, 200–205. <https://doi.org/10.1038/s41561-018-0297-z>
- Brocher, T. M. (2005) Empirical Relations between Elastic Wavespeeds and Density in the Earth's Crust. *Bulletin of the Seismological Society of America*. 95 (6): 2081–2092. <https://doi.org/10.1785/0120050077>
- Charles A. Langston, Donald V. Helmberger. (1975). A Procedure for Modelling Shallow Dislocation Sources, *Geophysical Journal International*. 42 (1), 117–130, <https://doi.org/10.1111/j.1365-246X.1975.tb05854.x>
- Chen, C. W., & Zebker, H. A. (2001). Two-dimensional phase unwrapping with use of statistical models for cost functions in nonlinear optimization. *J. Opt. Soc. Am. A*, 18(2), 338–351. <https://doi.org/10.1364/JOSAA.18.000338>
- Chen, Y., Meng, L., Zhang, A., & Wen, L. (2018). Source Complexity of the 2015 Mw 7.9 Bonin Earthquake. *Geochemistry, Geophysics, Geosystems*, 19. <https://doi.org/10.1029/2018GC007489>
- Chen, K., Avouac, J.-P., Geng, J., Liang, C., Zhang, Z., Li, Z., & Zhang, S. (2022). The 2021 Mw 7.4 Madoi Earthquake: An archetype bilateral slip-pulse rupture arrested at a splay fault. *Geophysical Research Letters*, 49, e2021GL095243. <https://doi.org/10.1029/2021GL095243>
- Dahlen, F. A. and Tromp, Jeroen. (2021). *Theoretical Global Seismology*, Princeton: Princeton University Press. <https://doi.org/10.1515/9780691216157>
- De Zan, F. (2014). Accuracy of Incoherent Speckle Tracking for Circular Gaussian Signals. *IEEE Geoscience and Remote Sensing Letters*, 11(1), 264–267. <https://doi.org/10.1109/LGRS.2013.2255259>
- Du, H. (2021). Estimating Rupture Front of Large Earthquakes Using a Novel Multi-Array Back-Projection Method. *Frontiers in Earth Science*, 9. <https://doi.org/10.3389/feart.2021.680163>
- Fattahi, H., Agram, P., & Simons, M. (2017). A Network-Based Enhanced Spectral Diversity Approach for TOPS Time-Series Analysis. *IEEE Transactions on Geoscience and Remote Sensing*, 55(2), 777–786. <https://doi.org/10.1109/TGRS.2016.2614925>
- Fialko, Y., Simons, M., & Agnew, D. (2001). The complete (3-D) surface displacement field in the epicentral area of the 1999 Mw7.1 Hector Mine Earthquake, California, from space geodetic observations. *Geophysical Research Letters*, 28(16), 3063-3066. <https://doi.org/10.1029/2001GL013174>
- Fielding, E. J., Z. Liu, O. L. Stephenson, M. Zhong, C. Liang, A. Moore, S.-H. Yun, and M. Simons (2020), Surface deformation related to the 2019 Mw 7.1 and Mw 6.4 Ridgecrest Earthquakes in California from GPS, SAR interferometry, and SAR pixel offsets, *Seismological Research Letters*, <https://doi.org/10.1785/0220190302>.

- Gardner, G. H. F., Gardner, L. W., & Gregory, A. R. (1974). Formation Velocity and Density—The Diagnostic Basics For Stratigraphic Traps. *Geophysics*, 39(6), 770–780. <https://doi.org/10.1190/1.1440465>
- Gisinger, C., Schubert, A., Breit, H., Garthwaite, M., Bals, U., Willberg, M., . . . Miranda, N. (2021). In-Depth Verification of Sentinel-1 and TerraSAR-X Geolocation Accuracy Using the Australian Corner Reflector Array. *IEEE Transactions on Geoscience and Remote Sensing*, 59(2), 1154-1181. <https://doi.org/10.1109/TGRS.2019.2961248>
- GMT China Community (2021). Retrieved from <https://github.com/gmt-china/china-geospatial-data>
- Han, S., Zhang, H., Xin, H., Shen, W., Yao, H. (2021). USTClitho2.0: Updated Unified Seismic Tomography Models for Continental China Lithosphere from Joint Inversion of Body-Wave Arrival Times and Surface-Wave Dispersion Data. *Seismological Research Letters*, 93 (1): 201–215. <https://doi.org/10.1785/0220210122>
- Hartzell, S., Liu, P., & Mendoza, C. (1996). The 1994 Northridge, California, earthquake: Investigation of rupture velocity, risetime, and high-frequency radiation. *Journal of Geophysical Research B: Solid Earth*, 101(9), 20091–20108. <http://pubs.er.usgs.gov/publication/70018152>
- Hersbach, H., Bell, B., Berrisford, P., Hirahara, S., Horányi, A., Muñoz-Sabater, J., . . . Thépaut, J.-N. (2020). The ERA5 global reanalysis. *Quarterly Journal of the royal meteorological society*, 146(730), 1999-2049. <https://doi.org/10.1002/qj.3803>
- Hong, S., Liu, M., Liu, T., Dong, Y., Chen, L., Meng, G., Xu, Y. (2022). Fault Source Model and Stress Changes of the 2021 Mw 7.4 Maduo Earthquake, China, Constrained by InSAR and GPS Measurements. *Bulletin of the Seismological Society of America*. <https://doi.org/10.1785/0120210250>
- Huang, R., Wang, Z., Pei, S., & Wang, Y. (2009). Crustal ductile flow and its contribution to tectonic stress in Southwest China. *Tectonophysics*, 473(3), 476–489. <https://doi.org/10.1016/j.tecto.2009.04.001>
- Ishii, M., Shearer, P. M., Houston, H., & Vidale, J. E. (2005). Extent, duration and speed of the 2004 Sumatra–Andaman earthquake imaged by the Hi-Net array. *Nature*, 435(7044), 933–936. <https://doi.org/10.1038/nature03675>
- Ji, C., Wald, D. J., Helmberger, D. V. (2002). Source Description of the 1999 Hector Mine, California, Earthquake, Part I: Wavelet Domain Inversion Theory and Resolution Analysis. *Bulletin of the Seismological Society of America*. 92 (4): 1192–1207. doi: <https://doi.org/10.1785/0120000916>
- Ji, C., Helmberger, D. V., Wald, D. J., and Ma, K.-F. (2003), Slip history and dynamic implications of the 1999 Chi-Chi, Taiwan, earthquake, *Journal of Geophysical Research*, 108, 2412, <https://doi.org/10.1029/2002JB001764>, B9.

Jiang, J., & Lapusta, N. (2016). Deeper penetration of large earthquakes on seismically quiescent faults. *Science*, 352(6291), 1293–1297. <https://doi.org/10.1126/science.aaf1496>

Jin, Z., & Fialko, Y. (2021). Coseismic and early postseismic deformation due to the 2021 M7.4 Maduo (China) earthquake. *Geophysical Research Letters*, 48, e2021GL095213. <https://doi.org/10.1029/2021GL095213>

Jolivet, R., Grandin, R., Lasserre, C., Doin, M. P., & Peltzer, G. (2011). Systematic InSAR tropospheric phase delay corrections from global meteorological reanalysis data. *Geophysical Research Letters*, 38(17), L17311. <https://doi.org/10.1029/2011GL048757>

Kame, N., & Yamashita, T. (1999). A new light on arresting mechanism of dynamic earthquake faulting. *Geophysical Research Letters*, 26(13), 1997–2000. <https://doi.org/10.1029/1999GL900410>

Kame, N., Rice, J., & Dmowska, R. (2003). Effects of prestress state and rupture velocity on dynamic fault branching. *Journal of Geophysical Research*, 108. <https://doi.org/10.1029/2002JB002189>

Kame, N., Yamashita, T. (1999) Simulation of the spontaneous growth of a dynamic crack without constraints on the crack tip path, *Geophysical Journal International*, 139(2): 345–358, <https://doi.org/10.1046/j.1365-246x.1999.00940.x>

Kato, A., Miyatake, T., Hirata, N. (2010) Asperity and Barriers of the 2004 Mid-Niigata Prefecture Earthquake Revealed by Highly Dense Seismic Observations. *Bulletin of the Seismological Society of America*. 100 (1): 298–306. doi: <https://doi.org/10.1785/0120090218>

Kato, A., & Igarashi, T. (2012). Regional extent of the large coseismic slip zone of the 2011 Mw 9.0 Tohoku-Oki earthquake delineated by on-fault aftershocks. *Geophysical Research Letters*, 39, 15301-. <https://doi.org/10.1029/2012GL052220>

Kennett, B. L. N. , Engdahl, E. R.. (1991) Traveltimes for global earthquake location and phase identification, *Geophysical Journal International*, 105(2), 429–465, <https://doi.org/10.1111/j.1365-246X.1991.tb06724.x>

Kiser, E., & Ishii, M. (2017). Back-Projection Imaging of Earthquakes. *Annual Review of Earth and Planetary Sciences*, 45(1), 271–299. <https://doi.org/10.1146/annurev-earth-063016-015801>

Lasserre, C., Peltzer, G., Crampé, F., Klinger, Y., Van der Woerd, J., and Tapponnier, P. (2005), Coseismic deformation of the 2001 $M_w = 7.8$ Kokoxili earthquake in Tibet, measured by synthetic aperture radar interferometry, *Journal of Geophysical Research*, 110, B12408, <https://doi.org/10.1029/2004JB003500>.

Li, B., Wu, B., Bao, H., Oglesby, D. D., Ghosh, A., Gabriel, A.-A., et al. (2022). Rupture heterogeneity and directivity effects in back-projection analysis. *Journal of Geophysical Research: Solid Earth*, 127, e2021JB022663. <https://doi.org/10.1029/2021JB022663>

- Li, Q., Wan, Y., Li, C., Tang, H., Tan, K. Dongzhen Wang (2022); Source Process Featuring Asymmetric Rupture Velocities of the 2021 Mw 7.4 Maduo, China, Earthquake from Teleseismic and Geodetic Data. *Seismological Research Letters*. doi: <https://doi.org/10.1785/0220210300>
- Liu, J., Hu, J., Li, Z., Ma, Z., Wu, L., Jiang, W., . . . Zhu, J. (2022). Complete three-dimensional coseismic displacements due to the 2021 Maduo earthquake in Qinghai Province, China from Sentinel-1 and ALOS-2 SAR images. *Science China Earth Sciences*, 65(1674-7313), 687. <https://doi.org/10.1007/s11430-021-9868-9>
- Liu, X., Chen, Q., Yang, Y., Xu, Q., Zhao, J., Xu, L., & Liu, R. (2022). The 2021 Mw7.4 Maduo earthquake: Coseismic slip model, triggering effect of historical earthquakes and implications for adjacent fault rupture potential. *Journal of Geodynamics*, 151, 101920. <https://doi.org/https://doi.org/10.1016/j.jog.2022.101920>
- Lohman, R. B., and Simons, M. (2005), Some thoughts on the use of InSAR data to constrain models of surface deformation: Noise structure and data downsampling, *Geochemistry, Geophysics, Geosystems*, 6, Q01007, <https://doi.org/10.1029/2004GC000841>.
- Lohman, R. B., and Barnhart, W. D. (2010), Evaluation of earthquake triggering during the 2005–2008 earthquake sequence on Qeshm Island, Iran, *Journal of Geophysical Research*, 115, B12413, <https://doi.org/10.1029/2010JB007710>.
- Mechie, J., S. V. Sobolev, L. Ratschbacher, A. Y. Babeyko, G. Bock, A. G. Jones, K. D. Nelson, K. D. Solon, L. D. Brown, and W. Zhao (2004), Precise temperature estimation in the Tibetan crust from seismic detection of the a-b quartz transition, *Geology*, 32, 601 – 604.
- Mendoza, C., & Hartzell, S. H. (1988). Aftershock patterns and main shock faulting. *Bulletin of the Seismological Society of America*, 78(4), 1438–1449. <https://doi.org/10.1785/BSSA0780041438>
- Meng, L., Inbal, A., and Ampuero, J.-P. (2011), A window into the complexity of the dynamic rupture of the 2011 Mw 9 Tohoku-Oki earthquake, *Geophysical Research Letters*, 38, L00G07, <https://doi.org/10.1029/2011GL048118>.
- Meng, L., Ampuero, J.-P., Stock, J., Duputel, Z., Luo, Y., & Tsai, V. C. (2012). Earthquake in a Maze: Compressional Rupture Branching During the 2012 Mw 8.6 Sumatra Earthquake. *Science*, 337(6095), 724–726. <https://doi.org/10.1126/science.1224030>
- Meng, L., Zhang, A., and Yagi, Y. (2016), Improving back projection imaging with a novel physics-based aftershock calibration approach: A case study of the 2015 Gorkha earthquake, *Geophysical Research Letters*, 43, 628– 636, <https://doi.org/10.1002/2015GL067034>.

- Meng, L., Bao, H., Huang, H., Zhang, A., Bloore, A., & Liu, Z. (2018). Double pincer movement: Encircling rupture splitting during the 2015 Mw 8.3 Illapel earthquake. *Earth and Planetary Science Letters*, 495, 164–173. <https://doi.org/10.1016/j.epsl.2018.04.057>
- Meng, L., Huang, H., Xie, Y., Bao, H., & Dominguez, L. A. (2019). Nucleation and kinematic rupture of the 2017 Mw 8.2 Tehuantepec earthquake. *Geophysical Research Letters*, 46, 3745–3754. <https://doi.org/10.1029/2018GL081074>
- Noda, H., & Lapusta, N. (2013). Stable creeping fault segments can become destructive as a result of dynamic weakening. *Nature*, 493(7433), 518–521. <https://doi.org/10.1038/nature11703>.
- Oliver-Cabrera, T., Jones, C. E., Yunjun, Z., & Simard, M. (2021). InSAR Phase Unwrapping Error Correction for Rapid Repeat Measurements of Water Level Change in Wetlands. *IEEE Transactions on Geoscience and Remote Sensing*, 60, 1-15. <https://doi.org/10.1109/TGRS.2021.3108751>
- Perrin, C., I. Manighetti, J.-P. Ampuero, F. Cappa, and Y. Gaudemer (2016), Location of largest earthquake slip and fast rupture controlled by along-strike change in fault structural maturity due to fault growth, *Journal of Geophysical Research: Solid Earth*, 121, 3666–3685, <https://doi.org/10.1002/2015JB012671>.
- Platt, J. D., J. W. Rudnicki, and J. R. Rice (2014), Stability and localization of rapid shear in fluid-saturated fault gouge: 2. Localized zone width and strength evolution, *Journal of Geophysical Research: Solid Earth*, 119, 4334–4359, <https://doi.org/10.1002/2013JB010711>.
- Rice, J. R. (2006), Heating and weakening of faults during earthquake slip, *Journal of Geophysical Research*, 111, B05311, <https://doi.org/10.1029/2005JB004006>.
- Robinson, D. P., Brough, C., and Das, S. (2006), The Mw 7.8, 2001 Kunlunshan earthquake: Extreme rupture speed variability and effect of fault geometry, *Journal of Geophysical Research*, 111, B08303, <https://doi.org/10.1029/2005JB004137>.
- Rosen, P. A., Gurrola, E., Sacco, G. F., & Zebker, H. (2012, 23-26 April 2012). The InSAR scientific computing environment. Paper presented at the EUSAR 2012.
- Sen, M. K., & Stoffa, P. L. (1991). Nonlinear one-dimensional seismic waveform inversion using simulated annealing. *GEOPHYSICS*, 56(10), 1624–1638. <https://doi.org/10.1190/1.1442973>
- Tobita, M., Nishimura, T., Kobayashi, T., Hao, K. X., & Shindo, Y. (2011). Estimation of coseismic deformation and a fault model of the 2010 Yushu earthquake using PALSAR interferometry data. *Earth and Planetary Science Letters*, 307(3), 430–438. <https://doi.org/10.1016/j.epsl.2011.05.017>

Di Toro, G., Han, R., Hirose, T., De Paola, N., Nielsen, S., Mizoguchi, K., Ferri, F., Cocco, M., & Shimamoto, T. (2011). Fault lubrication during earthquakes. *Nature*, 471(7339), 494–498.
<https://doi.org/10.1038/nature09838>

USGS. (2022). Retrieved from <https://earthquake.usgs.gov/earthquakes/eventpage/us7000e54r/moment-tensor>

Vallée, M., Landès, M., Shapiro, N. M., and Klinger, Y. (2008), The 14 November 2001 Kokoxili (Tibet) earthquake: High-frequency seismic radiation originating from the transitions between sub-Rayleigh and supershear rupture velocity regimes, *Journal of Geophysical Research*, 113, B07305,
<https://doi.org/10.1029/2007JB005520>.

Vallée, M., and Dunham, E. M. (2012), Observation of far-field Mach waves generated by the 2001 Kokoxili supershear earthquake, *Geophysical Research Letters*, 39, L05311, <https://doi.org/10.1029/2011GL050725>.

Wang, W., Fang, L., Wu, J., Tu, H., Chen, L., Lai, G., Zhang, L. (2021). Aftershock sequence relocation of the 2021 MS7.4 Maduo Earthquake, Qinghai, China. *Science China Earth Sciences (in Chinese)*,
<https://doi.org/10.1007/s11430-021-9803-3>

Wang, M., Shen, Z. K. (2020). Present-day crustal deformation of conti-nental China derived from GPS and its tectonic implications, *Journal of Geophysical Research*, 125(2), e2019JB018774,
<https://doi:10.1029/2019JB018774>.

Wang, M., Wang, F., Jiang, X., Tian, J., Li, Y., Sun, J., Shen, Z. (2022). GPS determined coseismic slip of the 2021 Mw7.4 Maduo, China, earthquake and its tectonic implication, *Geophysical Journal International*, 228(3), 2048–2055, <https://doi.org/10.1093/gji/ggab460>

Wen, Y., Ma, K., Song, T. A., Mooney, W. D. (2009) Validation of the rupture properties of the 2001 Kunlun, China (Ms = 8.1), earthquake from seismological and geological observations, *Geophysical Journal International*, 177(2), 555–570, <https://doi.org/10.1111/j.1365-246X.2008.04063.x>

Wu, SR., Li, GS., He, F., Zhang, YS., Shi, SJ., Han, JL., Zeng, LQ., (2002). Geometry and kinematics in the east segment of the surface rupture zone occurring during the Kunlun earthquake. *Geological Bulletin of China*, 21, 8-9

Xia, S., Shi, L., Li, Y., Guo, L. (2021). Velocity structures of the crust and uppermost mantle beneath the northeastern margin of Tibetan plateau revealed by double-difference tomography. *Chinese Journal of Geophysics (in Chinese)*, 64(9): 3194-3206, <https://doi.org/10.6038/cjg2021O0514>

Yao, H., Gerstoft, P., Shearer, P. M., and Mecklenbräuker, C. (2011), Compressive sensing of the Tohoku-Oki Mw 9.0 earthquake: Frequency-dependent rupture modes, *Geophysical Research Letters*, 38, L20310,
<https://doi.org/10.1029/2011GL049223>.

Yokota, Y., Kawazoe, Y., Yun, S., Oki, S., Aoki, Y., Koketsu, K. Joint inversion of teleseismic and InSAR datasets for the rupture process of the 2010 Yushu, China, earthquake. (2012). *Earth Planet Sp* 64, 1047–1051. <https://doi.org/10.5047/eps.2012.04.008>

Yue, H., Shen, Z.-K., Zhao, Z., Wang, T., Cao, B., Li, Z., Bao, X., Zhao, L., Song, X., Ge, Z., Ren, C., Lu, W., Zhang, Y., Liu-Zeng, J., Wang, M., Huang, Q., Zhou, S., & Xue, L. (2022). Rupture process of the 2021 M7.4 Maduo earthquake and implication for deformation mode of the Songpan-Ganzi terrane in Tibetan Plateau. *Proceedings of the National Academy of Sciences*, 119(23), e2116445119. <https://doi.org/10.1073/pnas.2116445119>

Yun, S. H., Zebker, H., Segall, P., Hooper, A., & Poland, M. (2007). Interferogram formation in the presence of complex and large deformation. *Geophysical Research Letters*, 34(12). <https://doi.org/10.1029/2007GL029745>

Yunjun, Z., Fattahi, H., & Amelung, F. (2019). Small baseline InSAR time series analysis: Unwrapping error correction and noise reduction. *Computers & Geosciences*, 133, 104331. <https://doi.org/10.1016/j.cageo.2019.104331>

Zhang, Z., Yuan, X., Chen, Y., Tian, X., Kind, R., Li, X., & Teng, J. (2010). Seismic signature of the collision between the east Tibetan escape flow and the Sichuan Basin. *Earth and Planetary Science Letters*, 292(3), 254–264. <https://doi.org/https://doi.org/10.1016/j.epsl.2010.01.046>

Zhang, X., Feng, W., Du, H., Samsonov, S., & Yi, L. (2022). Supershear rupture during the 2021 Mw 7.4 Maduo, China, earthquake. *Geophysical Research Letters*, 49, e2022GL097984. <https://doi.org/10.1029/2022GL097984>

Zhu, S., Yuan, J. (2020) Physical mechanism for severe seismic hazard in the 2010 Yushu, China, earthquake (Mw= 6.9): insights from FEM simulations, *Geomatics, Natural Hazards and Risk*, 11:1, 2123-2146, <https://doi.org/10.1080/19475705.2020.1832150>